Corrosion Science 163 (2020) 108255

Contents lists available at ScienceDirect

Corrosion Science

journal homepage: www.elsevier.com/locate/corsci

Corrosion behaviors of Zr-Sn-Nb-Fe-Mo alloys in pure water at 360 °C/18.6 MPa: Influence of annealing temperature on the anti-corrosion properties

Huigang Shi[a], Jiuxiao Li[b,*], Jianwei Mao[a], Weijie Lu[a,*]

[a] State Key Laboratory of Metal Matrix Composites, School of Material Science and Engineering, Shanghai Jiao Tong University, Shanghai, 200240, PR China
[b] School of Materials Engineering, Shanghai University of Engineering Science, Shanghai, 201620, PR China

ARTICLE INFO

Keywords:
Zirconium alloys
Raman spectroscopy
Crack formation
Corrosion resistance
Stress distribution

ABSTRACT

Zr-Sn-Nb-Fe-Mo alloys are heat treated at two different temperatures (480 and 550 °C). A better corrosion resistance is obtained when annealed at 550 °C. The lower oxidation rate is attributed to the reduction of oxide grain boundary area, as the grain boundaries are the most common short-circuiting paths for oxygen diffusion. Two mechanisms are responsible for crack formation in the oxide: phase transition from tetragonal to monoclinic and delayed oxidation of precipitates. The cracks are generated continuously and linked together to form long cracks, leading to the delamination of oxide films and stress relaxation in the oxide.

1. Introduction

Aqueous corrosion of zirconium alloys has become the major factor limiting prolonged fuel campaigns in nuclear industry [1–4]. The oxide films form on the surface of zirconium alloys during waterside corrosion at high temperature and high pressure, and then grow inwards by the diffusion of O ions through the crystallite boundary or the bulk of oxide grains [5–8]. Initially, the oxide layers have a protective nature, leading to a decreasing oxidation rate [9,10]. The corrosion kinetics primarily follow a parabolic or cubic law [11–13]. At a certain oxide thickness, regions of the previously protective oxide break down, eventually resulting in an increased corrosion rate, which is commonly known as transition in corrosion kinetics [14–16]. The protective oxide will then build up again, resulting in cyclic oxidation kinetics until a regime of accelerated linear growth is reached.

It is well known that the properties of zirconium alloys depend basically on their chemical compositions [17–25]. Based on in-reactor experience of various Zr-based alloys, the important elements in commercial zirconium alloys such as ZIRLO and M5 tubes are Sn and Nb [17–21]. It is commonly accepted that Sn was originally added to zirconium alloys to counter the poor corrosion resistance caused by nitrogen. In N-free zirconium alloy, however, Sn has been found to deteriorate the corrosion resistance [17,18]. Thus, the modern trend of Zr-based alloy design is to reduce Sn content, but only slightly (from 1.0–1.7% to 0.4–0.6%), in order to maintain the good creep properties [26]. Nb is found to increase the corrosion and irradiation-induced growth resistance, and it was introduced to ZIRLO and M5 tubes to improve the corrosion resistance with a good creep resistance [19,20,27]. Fe has been playing important roles in the development of zirconium alloys for nuclear applications [28–30]. The effect of Fe on the corrosion resistance of zirconium alloys is mainly controlled via the type and distribution of the second phase particles [31]. In the modern design of zirconium alloys, Fe element is generally added to improve the corrosion resistance. Mo is one of the promising alloying elements to achieve better performance in zirconium alloys. The Mo addition can increase the creep resistance [32], enhance the yield strength [33] and improve the corrosion resistance via proper heat treatment [34]. The Mo addition was previously recommended to be limited to 0.1%.

On the other hand, the microstructure of alloys has a profound influence on the corrosion behaviors under conditions of high temperature and high pressure. A number of work has been implemented to correlate the microstructure of zirconium alloys with their corrosion behaviors. Yao [35] studied the effect of final annealing condition on the corrosion behavior of Zircaloy-4 in lithiated water and found that the corrosion resistance got worse with increasing annealing temperature in the range of 480–600 °C. Ni [36] demonstrated that the final heat treatment had minor influence on the oxidation kinetics for ZIRLO alloy. Kim [37] investigated the variation of microstructure and corrosion characteristics with different annealing temperature (540–660 °C) for HANA-4 (Zr-1.5Nb-0.4Sn-0.2Fe-0.1Cr) alloy. They found that the corrosion resistance increased with the increase of annealing temperature. However, Park [38] reported an opposite trend

* Corresponding authors.
E-mail addresses: lijiuxiao@126.com (J. Li), luweijie@sjtu.edu.cn (W. Lu).

https://doi.org/10.1016/j.corsci.2019.108255
Received 19 May 2019; Received in revised form 23 August 2019; Accepted 3 October 2019
Available online 04 October 2019
0010-938X/

that, HANA-4 alloy with lower final annealing temperature had better corrosion resistance at 360 °C in pure water autoclave.

It was found that the impact of microstructure variation on the corrosion behavior for different commercial zirconium alloys is different. In this paper, a new Zr-Sn-Nb-Fe-Mo alloy was designed for nuclear cladding and it possessed surprisingly better corrosion resistance than ZIRLO™ alloy. In order to establish some correlations between microstructure variation and corrosion resistance of alloys, two different annealing temperatures were selected and two kinds of microstructure were obtained. A detail characterization of the microstructural features including grain size, degree of recrystallization, oxide cross-sectional microstructure and phase composition of oxide films formed on samples was carried out.

2. Experimental

2.1. Material preparation

Zr-Sn-Nb-Fe-Mo alloy was processed by vacuum arc re-melting for three times to obtain chemical homogeneity. The alloy contains 0.34% Sn, 0.74% Nb, 0.31% Fe, 0.14% Mo, 0.11% O and with Zr as the balance (in wt. %). The manufacturing process of the experiment alloys comprised of a hot forging at 1000 °C for 1 h, a β-quenching at 1050 °C for 30 min, a hot rolling at 600 °C, and four times of cold rolling followed by an annealing. The sequence of the heat treatments was illustrated in Fig. 1. The specimens were divided into two groups (denoted as sample 1 and 2) by different annealing temperature. For sample 1, the intermediate annealing was conducted at 550 °C for 4 h and the final annealing condition was 550 °C for 5 h. By contrast, a much lower annealing temperature was carried out in sample 2 (480 °C/4 h for the intermediate annealing and 480 °C/5 h for the final annealing).

2.2. Corrosion test

Rectangular specimens of (25 × 15 × 0.6) mm^3 were prepared from sample 1 and 2. Prior to the autoclaving tests, all the samples were chemically polished using a pickling solution (10% HF, 30% HNO_3, 30% H_2SO_4 and 30% H_2O, in volume), sequentially rinsed in pure water, boiling deionized water and then blow-dried with warm air. Corrosion testing was performed in a static autoclave in pure water up to 300 days at 360 °C and saturation pressure, corresponding to 18.6 MPa at this temperature according to ASTM G2-88. Autoclaving tests of different durations were performed determining in each case the weight gain per unit area of the specimens. The weight gain was averaged from 6 specimens.

2.3. Microstructure characterization

The microstructure of the annealed specimens before corrosion tests were characterized by electron back-scatter diffraction (EBSD) analysis system (Channel 5, AZtec HKL Max), installed on a Mira 3 SEM scanning electron microscope. EBSD data for each sample were collected at step size of 0.2 μm with a scanning area of 90 × 130 μm^2 on the surface. The cross-sections of oxide films were characterized by SEM (JEOL-7800F, Japan) and TEM (JEOL-2100F, Japan). The fractured cross-section of oxide films for SEM observation were prepared by breaking the oxide on the edge of the samples after etching in the solution (H_2O:HNO_3:HF = 9:9:2) for 20 min to dissolve the metal substrates. The cross-section of oxide scales for SEM analysis in back-scattered electron (BSE) mode was ground according to standard metallographic techniques. Before SEM observations, the cross-sections were coated with a gold layer to improve the surface conductivity of the oxide films. The cross-sectional samples of the oxides for TEM observation were prepared using a FEI Scios focused ion beam (FIB) in situ lift-out technique [39,40]. The different phases in the oxide films were characterized by Raman spectroscopy (LabRAM HR Evolution, France) using a 532 nm excitation line of a solid laser. Spectra were acquired using a 50× (NA = 0.75) objective. Before each analysis, the incident power of 10 mW was used to avoid excessive heating of the samples. The wavenumber accuracy is about 0.1 cm^{-1} and the acquisition times of individual spectra were in the 20–30 s range, depending on the signal/noise ratio needed. For each sample, systematic area scans with a step size of 0.3 μm were performed on the polished cross-sections of the oxides to study the variations in oxide crystal structure and composition as a function of position in the oxide thickness. The Raman images was obtained using band fitting procedures, and each line of interest is fitted with a mixed Gaussian-Lorentzian line shape to take into account instrumental broadening.

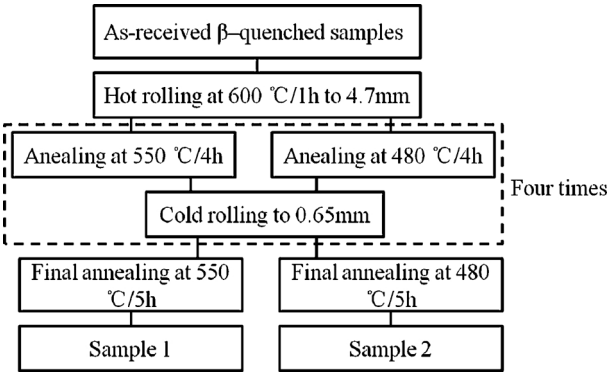

Fig. 1. Schematic of the heat treatment history of experimental alloys.

3. Results

3.1. Characteristics of microstructure of the experimental alloys

Fig. 2 exhibits the inverse pole figure (IPF) maps, grain boundary (GB) maps and mis-orientation angle distribution (MAD) histograms derived from EBSD data for both groups. As shown in the IPF maps, sample 1 is mainly composed of well-equiaxed grains, as well as some fine grains (less than 0.5 μm) around them after 550 °C/5 h heat treatment. Meanwhile, the orientations (colors) of some grains are non-uniform according to the standard triangle at the bottom of Fig. 2. It is assumed that these non-uniform grains are usually caused by the insufficient annealing time or low annealing temperature. After 480 °C/5 h treatment, the apparent long strip structure along the rolling direction (RD) is observed in sample 2, and a large number of fine grains are observed as well. Meanwhile, the orientation (color) non-uniformities are also confirmed in most of the grains. It is believed that these long strip structures and distorted grains are the remnant products by cold rolling, implying that recrystallization degree is very low in sample 2. The average grain size is reduced by the decrease of annealing temperature, from 2.8 μm to 1.5 μm. With respect to GB maps, it is worth noting that nearly half of GBs possess low angle grain boundaries (LAGBs, marked as sky-blue line) for sample 1, whereas the LAGBs are predominant in the GB maps for sample 2. Hence, it is confirmed that the degree of recrystallization in sample 1 is significantly higher than that in sample 2, which is caused by a lower annealing temperature. The MAD histograms exhibit a quantitative result for the grain mis-orientation angle for two groups. It is clear that the fraction of LAGBs gradually increases from 50.7% to 81.3% with the decrease of annealing temperature. In general, the sub-grains will coalesce together by grain boundaries migration and dislocation slip during the annealing process, leading to the recrystallization nucleation behavior. The equiaxed grains are formed by the growing of sub-grains, then replacing the deformed structure. Consequently, the higher the annealing temperature, the higher the recrystallization degree.

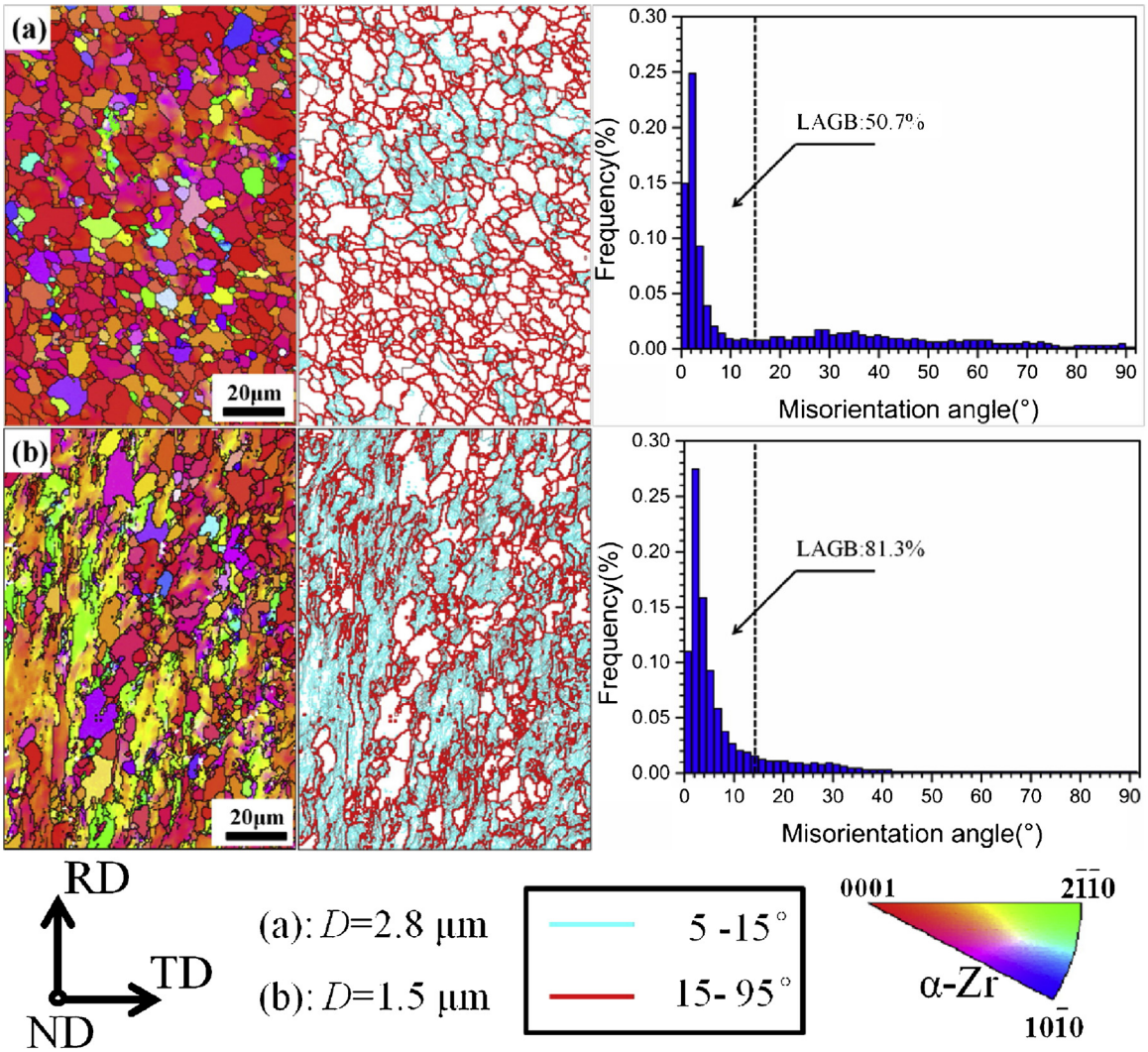

Fig. 2. EBSD inverse pole figure (IPF) map, grain boundary (GB) map and mis-orientation angle distribution (MAD) in the samples for (a) 550 °C/5 h and (b) 480 °C/5 h, respectively.

3.2. Corrosion kinetics of experimental alloys

Fig. 3 shows the corrosion weight gain of the two groups as a function of exposure time in deionized water at 360 °C/18.6 MPa for 300 days. The weight gains of both groups follow a parabolic law before the transition in the oxidation kinetics. The oxidation rate of sample 2 is higher than that of sample 1, and the gap of weight gain between them becomes larger as the exposure time increases. An abrupt increase in weight gain is observed after 200-day exposure in sample 2 (black arrow), indicating that the oxidation transition occurred. While in sample 1, there is no sudden increment in weight gain until 260-day exposure (red arrow). Hence, it can be concluded that the oxidation transition time for sample 1 and 2 are almost 260 and 200 days, respectively. Sample 1 possesses a relatively better corrosion resistance than sample 2 in deionized water at 360 °C/18.6 MPa.

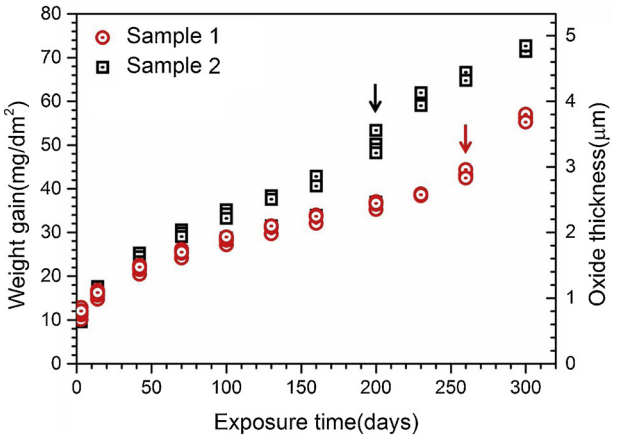

Fig. 3. Weight gain in mg/dm^2 versus exposure time for the corrosion of experimental alloys in pure water at 360 °C/18.6 MPa. (For interpretation of the references to colour in the text, the reader is referred to the web version of this article.)

3.3. SEM observation of the oxide appearance

Fig. 4 shows the cross-sections of the oxide films formed on both groups. At exposure time of 100 days, large columnar grains and small equiaxed grains are clearly observed in the oxide film formed on both groups (Fig. 4a and e). The equiaxed grains are formed in the outer part of the oxide film, whereas the columnar grains are situated in the inner part, aligning in the oxide growth direction and growing perpendicular to the O/M interface. The equiaxed grains are 20–50 nm in diameter, and the columnar grains are 300–700 nm in length and 50–100 nm in width. With up to 200 days, a few micro-pores are observed in oxide

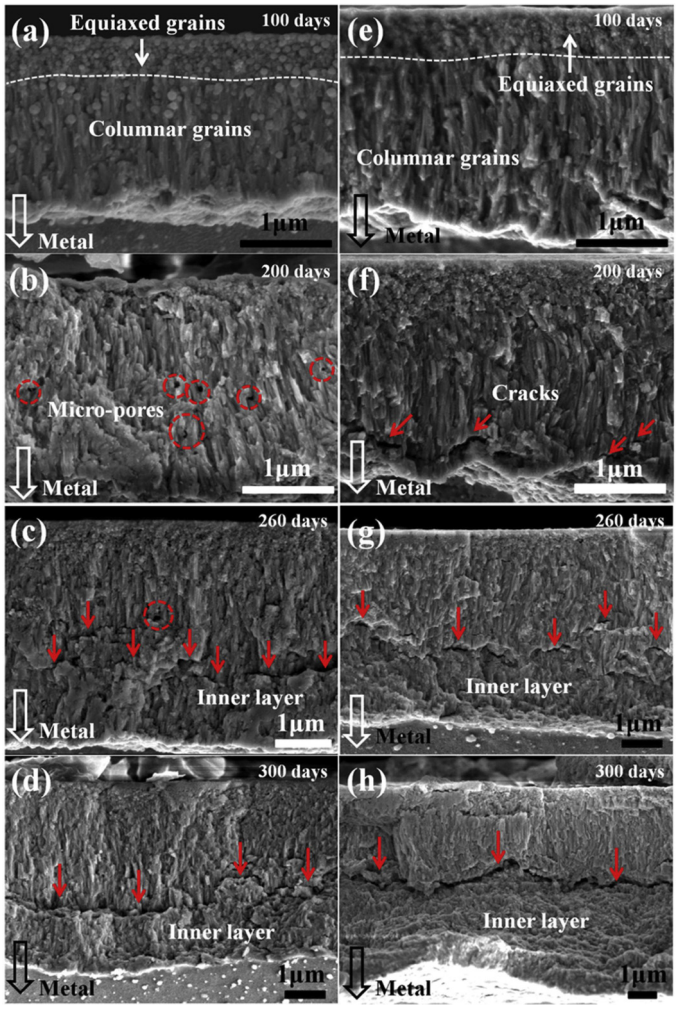

Fig. 4. Cross-sectional morphology of the oxide films formed on both samples: (a)–(d) 100-day, 200-day, 260-day and 300-day exposure for sample 1, respectively; (e)–(h) 100-day, 200-day, 260-day and 300-day exposure for sample 2, respectively. (For interpretation of the references to colour in the text, the reader is referred to the web version of this article.)

Table 1
Statistical data about oxide thickness from SEM observation in both samples.

Alloy	Exposure time (days)	Pre/Post-transition	Oxide thickness (μm)		
			Total	Inner layer	Outer layer
Sample 1	100	Pre-transition	1.8–2.1	–	–
	200	Pre-transition	2.1–2.5	–	–
	260	Post-transition	3.5–3.9	0.9–1.3	2.6–2.8
	300	Post-transition	4.1–4.5	1.4–1.6	2.8–3.1
Sample 2	100	Pre-transition	2.3–2.5	–	–
	200	Post-transition	2.6–3.0	0.2–0.5	2.3–2.5
	260	Post-transition	4.4–5.0	1.4–2.3	2.5–2.9
	300	Post-transition	6.4–7.5	2.9–3.9	3.2–4.0

film of sample 1 (marked by red circles in Fig. 4b), while several lateral cracks can be observed near the oxide/metal interface in the film of sample 2 (marked by red arrows in Fig. 4f). As exposure time increases to 260 days, some long cracks are clearly observed in both groups, and the oxide films are divided into two layers (red arrows in Fig. 4c and g). The discrepancy between them is that the inner layer of oxide film in sample 2 is thicker than that in sample 1, while the outer layers in both samples have the same thickness. The inner layer is almost composed of large columnar grains, which is believed to have a protective nature. The long cracks in both samples allow for the ingression of pure water through the oxide films, and the O oxidizing species can move parallel to the oxide/metal interface, resulting in an increased oxidation rate in water. The similar characteristics are more evident in both samples after 300 days' exposure time (Fig. 4d and h), and the inner layer of oxide grows thicker as the exposure time increases. Table 1 listed the statistical data about oxide thickness from SEM observation. It can be found that the oxide film in sample 1 is relatively thinner than that in sample 2 at the same exposure time, indicative of a slower oxidation rate for sample 1.

The features of the oxide films were also examined in cross-section using SEM in back-scattered electron (BSE) mode. At exposure time of 100 days, no visible cracks are detected in sample 1, while a continuous oxide layer with some cracks is observed in the oxide film of sample 2 (Fig. 5a and e). With up to 200 days, it is important to note that some long cracks are observed in the oxide of sample 2 (marked as white arrow) and it is near to the transition time (Fig. 5f). In sample 1, however, only few and tiny cracks are observed in the oxide, which is prior to the transition time (Fig. 5b). The number of the lateral cracks increase with the extension of exposure time in both samples. The oxide film on sample 1 possesses obviously less number of cracks than that in sample 2 at the same exposure time. After 260 and 300 exposure days, most of the cracks are inter-connected to form long cracks, result in the layering of the oxide scales (Fig. 5c–d and g–h). Accordingly, it can be deduced from Fig. 5 that the transition time of oxidation occurs at about 200 days for sample 2, whereas the transition time for sample 1 is about 260 days.

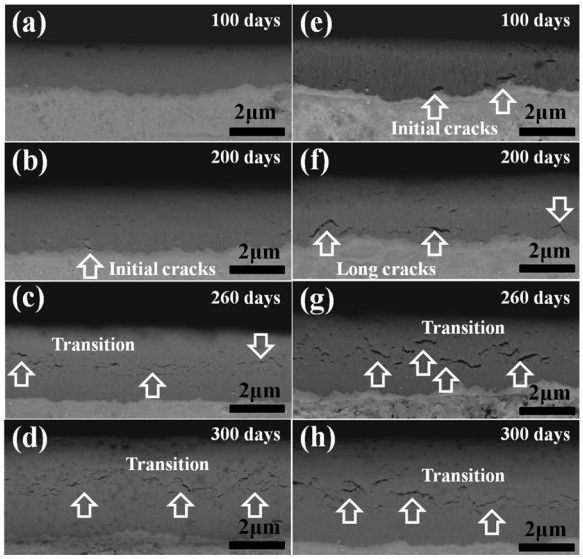

Fig. 5. Back-scattered electron mode SEM images representative of the oxide (cross-section): (a–d) 100, 200, 260 and 300 days' exposure for sample 1, respectively; (e–h) 100, 200, 260 and 300 days' exposure for sample 2, respectively.

3.4. TEM analysis on the morphology and structure of oxides

To further characterize the cross-sectional morphology of oxide scales, TEM observation was applied in the specimens. Fig. 6 shows the cross sectional TEM micrograph of the oxide formed on both groups in pure water after 200 exposure days. Note that typical grain morphologies of oxide films are exhibited in both groups: large columnar grain structure in the inner part and small equiaxed grain towards the outer part. The diameter of the equiaxed grains is 10–50 nm; the length and width of columnar grains are 70–500 nm and 20–140 nm, respectively. A large number of micro-pores (marked as red ellipse) are observed in the outer surface in both groups, corresponding to the porous area of equiaxed grains (Fig. 6c and e). This area is generally 500 nm in width and is commonly correlated with the fast corrosion rate at the initial stage of zirconium alloy oxidation [41]. For sample 1, small cracks (marked as red arrows) are observed with length of 50–200 nm in the oxide, which are parallel to the O/M interface. In addition, some tiny cracks are observed on the side of the precipitate opposite to the oxide/metal (O/M) interface, as marked by the red circles in Fig. 6b. For sample 2, more cracks are examined in the TEM image and some of them link together to form long cracks (Fig. 6d-h). The length of these cracks can reach to several microns, which are easy path for water to ingress. The highly oriented columnar grains are aligned tightly in the inner part of oxide (marked as dashed lines in Fig. 6g–h), with some micro-cracks observed close to the O/M interface (marked as red circles, same to the feature in Fig. 6b).

Figs. 7 and 8 show the HRTEM images of oxide grain morphology on sample 1 and 2 at 200 days' exposure time, respectively. The monoclinic zirconia is detected at different areas of the oxide depth such as the outer surface (the domains A–C in Figs. 7a and 8 a), middle oxide layer (the domains D–F in Figs. 7b and 8 b), and the O/M interface (the domains I–J in Fig. 7c and G in Fig. 8c). The tetragonal zirconia is found only at the O/M interface (the domains G–H in Fig. 7c and H–I in Fig. 8c). As shown in Fig. 7, equiaxed grains are 15–20 nm in size and semi-coherent grain boundaries are formed between grain B and C. This can be attributed to the lattice misfit by many dislocations around them. In the middle region, columnar grains are aligned tightly. The boundary between grain D and E is completely coherent without any deviation and can be seen as one columnar grain. Micro-cracks can be seen between grain D and F, with some dislocations formed in the grain boundaries. At the O/M interface, the oxide grains G and H are revealed as a tetragonal phase. The IFFT results from the regions I and J indicate that some dislocations were observed in the monoclinic phase. Similar results are obtained in sample 2, as shown in Fig. 8. Note that large columnar grains in the middle region are closely arranged in the oxide

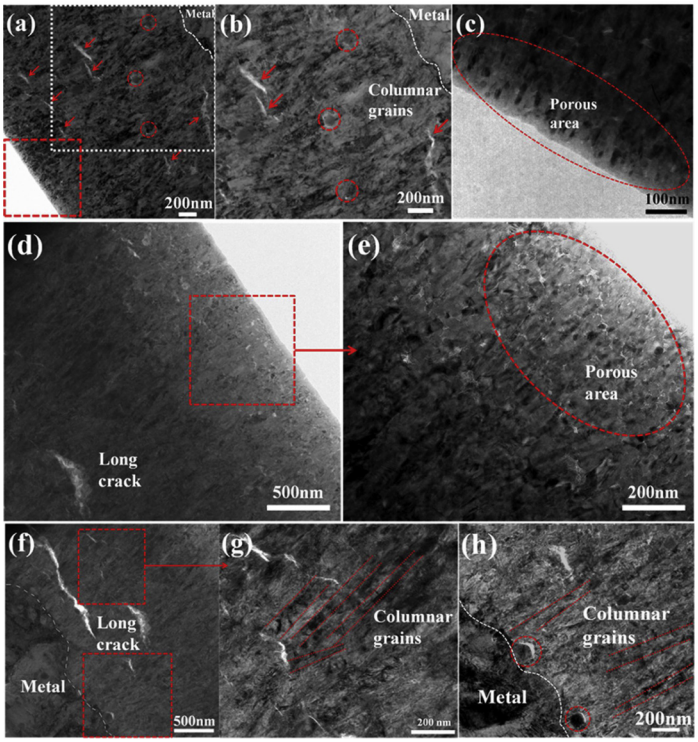

Fig. 6. TEM images of the cross-sectional morphology of oxide films in both groups after 200 days' exposure: (a–c) the morphology of oxide formed on sample 1; (d–h) the morphology of oxide formed on sample 2. (For interpretation of the references to colour in the text, the reader is referred to the web version of this article.)

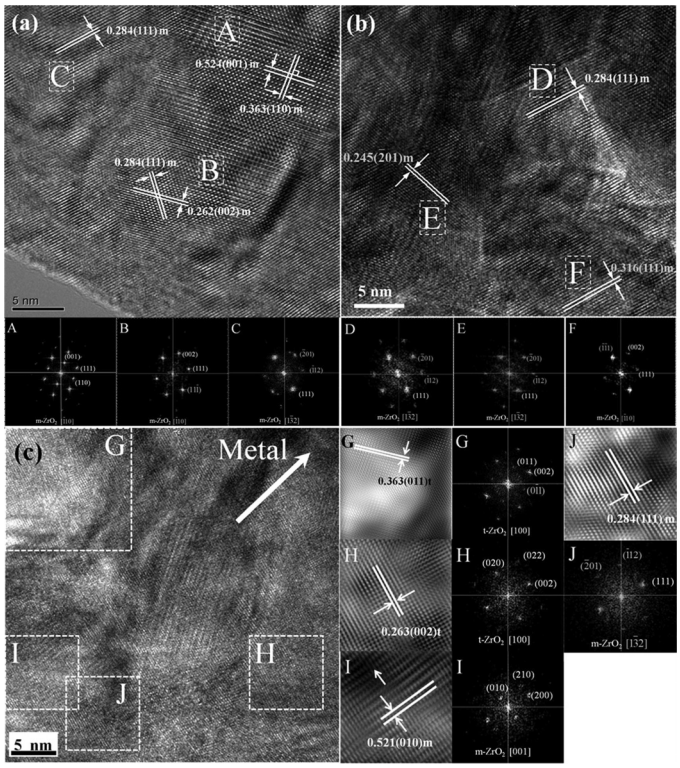

Fig. 7. HRTEM images for the cross-sectional morphology of oxide films in sample 1 after 200 days' exposure: (a) the outer surface of oxide; (b) the middle part of oxide; (c) the O/M interface. The white arrow indicates the approximate direction of oxide growth. The Fast Fourier Transform (FFT) and Inverse Fast Fourier Transform (IFFT) diffraction patterns are for the square regions A–J marked in (a)–(c).

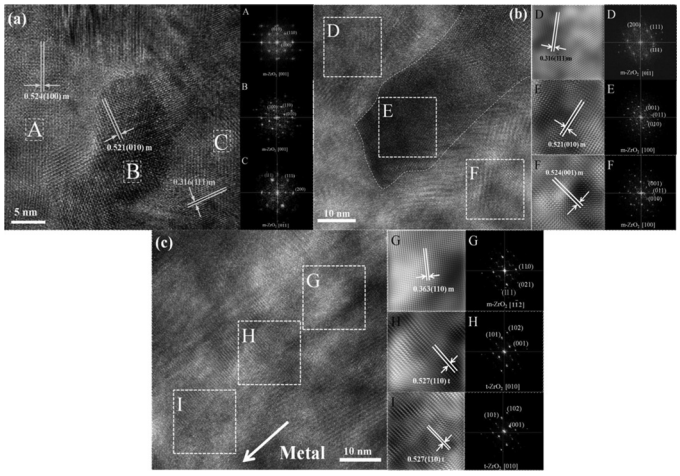

Fig. 8. HRTEM images for the cross-sectional morphology of oxide films in sample 2 after 200 days' exposure: (a) the outer surface of oxide; (b) the middle region of oxide; (c) the O/M interface. The white arrow indicates the approximate direction of oxide growth. The FFT and IFFT diffraction patterns are for the square regions A–I marked in (a)–(c).

growth direction and growing perpendicular to the O/M interface (marked as dashed lines in Fig. 8b).

3.5. Raman spectroscopy analysis on the oxide scales

Raman spectroscopy has been used as a method to characterize the various phases involved in the corrosion of zirconium alloys [42–44]. This technique measures the wavelength shift due to inelastic scattering of photos incident on the sample, the degree of which depends on the molecular nature of the materials. In this work, specimens for both groups after 200 days' exposure were investigated using Raman spectroscopy as described above. To create the 2D spectral images, the Raman data was processed using the LabSpec 5.0 software. Firstly, the baseline was subtracted by the way of linear fitting or polynomial fitting, and the integrate intensity of all the spectra was normalized to unity and computed for each studied peak. Then, the peak position of interest for all the spectra was fitted with a mixed Gaussian-Lorentzian line shape to take into account instrumental broadening. The different resulting images clearly show where the different phases are located. In our study, the 280 cm^{-1} and 189 cm^{-1} peak were used to create the phase distribution of t-ZrO_2 and m-ZrO_2 in the oxide, respectively. Fig. 9 shows the typical Raman spectra of oxide film close to the O/M interface formed on sample 1. The more intense of the Raman peaks are located at 177, 189, 475 cm^{-1} (identified as monoclinic phase) and a weak Raman peak of tetragonal phase is detected at 280 cm^{-1} position. Fig. 10 displays the phase distribution of cross-section of oxide formed on both groups after 200 days' exposure. Results show that a higher tetragonal phase fraction is observed near the O/M interface (Fig. 10a and c), whereas the monoclinic phase is predominant in the oxide films for both groups (Fig. 10b and d). This result is consistent with our TEM observation. As the oxide grows into the metal, the newly formed oxide usually consists of tetragonal and monoclinic phase, and the tetragonal phase will transform into monoclinic phase at some distance from the interface [45,46].

Fig. 11 shows the Raman peak shifts of 189 cm^{-1} line and the corresponding stress magnitude on the cross section of oxide films

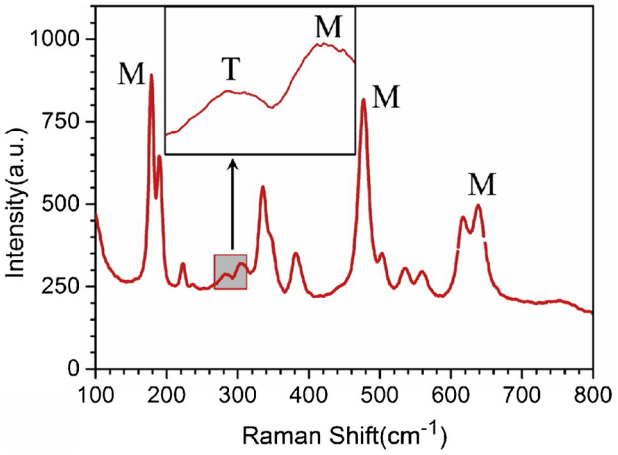

Fig. 9. Typical Raman spectra near the O/M interface formed on sample 1, which was oxidized at 360 °C/18.6 MPa for 200 days. M and T represent monoclinic phase and tetragonal phase, respectively.

formed on both groups after 200 days' exposure. The stress magnitude and distribution in the oxide film can be calculated by multiplying a stress shift coefficient, which has a value of 2.49 cm/GPa [43] or 0.528 GPa/cm [47]. It is clearly shown that a stress gradient throughout the oxide scale is present and the compressive stress is highest at the O/M interface in sample 1. The plausible reason for this gradient of stress is caused partly by creep in the metal substrate [48] and the gradually formation of cracks [49]. The magnitude of compressive stress is about 1.3 GPa at the O/M interface, which may effectively contribute to the stabilization of the tetragonal phase [50]. For sample 2, a steeper stress gradient is obtained on the cross section of oxide films, from 0.031 GPa at the outer surface to 1.6 GPa at the O/M interface. It has been proposed that a steeper stress gradient usually results in a weaker resistance to breakaway for the oxide films [51], indicating that sample 2 possesses a relatively worse corrosion resistance than sample 1. The compressive stress magnitudes measured in our samples are consistent with the stress values obtained by Bouvier (1.5 GPa) [52] and Godlewsk (0.2–1.5 GPa) [53] on Zr-4 alloy under steam using Raman spectroscopy, and also those obtained by Polatidis (0.7–1.5 GPa) [54] and Preuss (1–1.5 GPa) [15] using synchrotron X-ray diffraction. Besides, a significant stress relaxation is observed in the oxide, with a distance of

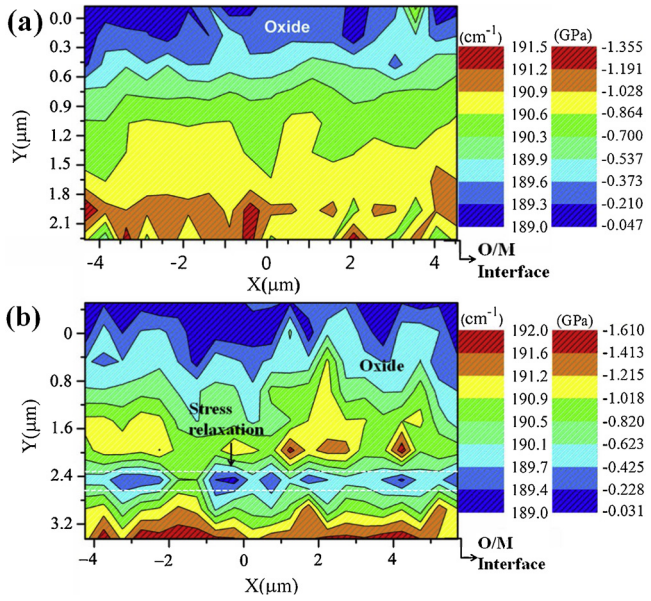

Fig. 11. Raman peak shifts of 189 cm^{-1} line and the corresponding stress magnitude on the cross section of oxide films on both samples after 200 days' exposure: (a) sample 1; (b) sample 2.

~0.8 μm away from the O/M interface (Fig. 11b). The relaxation phenomenon has been reported by many researchers in zirconia scales and the possible mechanical factors include oxide or metal creep [48], hydrogen induced lattice strain [55], or crack formation in the oxide layers [56]. However, finite element analysis by Platt [57] suggested that the impact of oxide creep is trifling and the influence of both creep and hydrogen-induced lattice strain in the metal too weak to explain the observed stress relaxation. Thus, the more possible reason for the relaxation could be attributed to the presence of long cracks in the area of oxide (Figs. 4f, 5 f and 6 f). As is seen from Figs. 5f and 6 f, some long cracks are located hundreds of nanometers away from the O/M interface, corresponding to the position of stress relaxation in the oxide. These long cracks relax the oxide and make it divide into two layers, resulting in the presence of two distinct stress gradients.

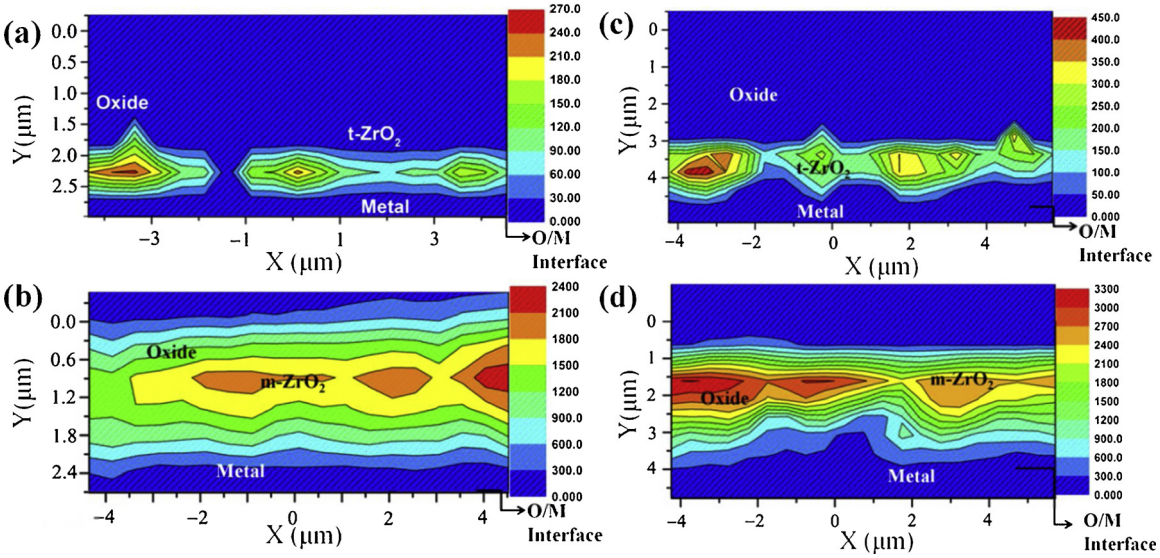

Fig. 10. Location of the m-ZrO_2 and t-ZrO_2 in the cross section of oxide scales formed on both groups after 200 days' exposure: (a)–(b) t-ZrO_2 and m-ZrO_2 distribution for sample 1, respectively; (c)–(d) t-ZrO_2 and m-ZrO_2 distribution for sample 2, respectively.

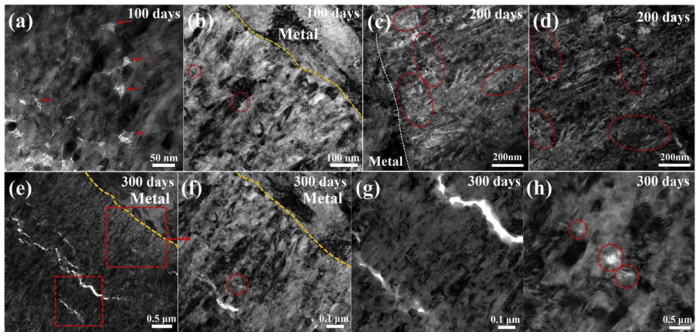

Fig. 12. TEM images of the cross-sectional morphology of oxide films formed on sample 1 with different exposure time: (a–b) after 100 days' exposure time; (c–d) after 200 days' exposure time; (e–h) after 300 days' exposure time. (For interpretation of the references to colour in the text, the reader is referred to the web version of this article.)

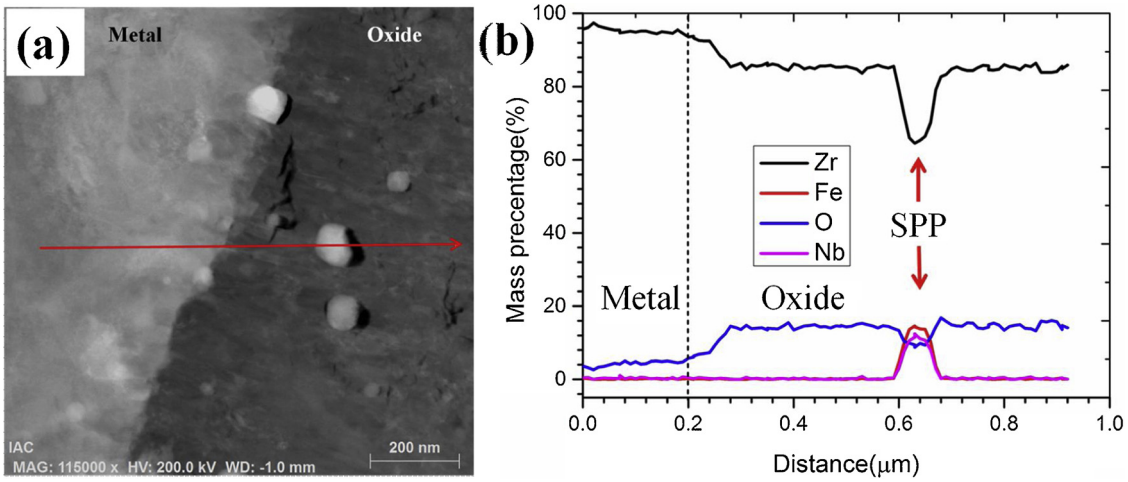

Fig. 13. (a) HADDF image of cross-sectional oxide films at O/M interface formed on sample 1 after 200 days' exposure time; (b) the corresponding EDS results along the path of red arrow in (a). (For interpretation of the references to colour in this figure legend, the reader is referred to the web version of this article.)

4. Discussion

4.1. Two mechanisms for the crack formation

It is widely accepted that the formation of pores and cracks is the precondition for the degradation of oxides, which will finally result in the transition of oxidation kinetics for zirconium alloys [58,59]. The cracks or interconnected porosity in oxide scales are important as they will provide fast tracks for diffusing species. According to the literatures, the appearance of lateral cracks in the oxide is correlated with the O/M interface roughness [60] or the large compressive stress [61]. A good consensus has been reached in recent years by researchers that a higher tetragonal fraction often results in a better corrosion resistance, or a longer pre-transition time in the zirconium alloys [8,44,62]. During the formation of zirconia scales, either tetragonal or monoclinic grains will firstly be formed at the O/M interface [63]. As shown in Fig. 12a, a thin layer (300–500 nm) is formed in the outer part of oxide, with small equiaxed grains and high levels of porosity. The newly formed grains will be properly oriented for growth under the effect of large compressive stress, and a high content of tetragonal zirconia could be stabilized by the compressive stress. Thus, a dense and will-developed columnar structure will be formed close to the O/M interface, as shown in Fig. 12b. As the oxide grows inwards, the tetragonal columnar grains will grow to a critical length when the compressive stress will not able to stabilize them, since the O/M interface is gradually to drive away from the previously formed oxide. Then the tetragonal grains will transform into monoclinic. It is well known that this phase transformation is highly correlated with volume expansion (3–7%) [49] and large shear strain (14–18%) [45]. Platt [64] simulated the tetragonal to monoclinic transformation during oxidation and found that both the dilatation and shear processes can cause stress concentrations in the surrounding oxide, allowing for an initiation site for the formation of lateral cracks. Bossis [65] found evidence of nano-cracks along the grain boundary between column grains, and suggested that the nano-cracks were correlated with the tensile stresses generated due to shear in the phase transformation. As shown in Fig. 12b, some nano-cracks (red circles) are observed between the column grain boundaries, which is consistent with previous studies. Therefore, it is assumed that the tetragonal-to-monoclinic phase transformation would result in crack formation during oxidation. As the oxidation progresses, more and more nano-cracks will generate in the oxide as the phase transformation occurs all the time. Fig. 12c and d shows the TEM morphology of the oxide grains at the innermost and middle part of the oxide scale after 200 days' exposure time. It is clear that the columnar grain structure predominates in these region, while lots of nano-cracks are also found (red circles). These cracks are 20–50 nm in length and are believed to be triggered by the tetragonal-to-monoclinic phase transformation. Similar features can be observed in the oxide films after 300 days' exposure, as shown in Fig. 12f and h. Besides, the oxide film is divided into two layers by the long cracks, which are formed by the interconnection of nano-cracks (Fig. 12e and g).

On the other hand, the precipitates will be incorporated into the oxide and some crescent shaped cracks are frequently observed at the precipitate-oxide interface towards the outer surface [66]. Fig. 13 exhibits the HADDF image of cross-sectional oxide films formed on sample 1 after 200 days' exposure time and the corresponding EDS analysis. The path of line scan crosses over the precipitate from metal to the oxide scale (red arrow in Fig. 13a). It is shown that micro-cracks are formed on the top of precipitates (white arrows in Fig. 13a). The O and Zr contents are decreased abruptly, while Fe and Nb contents are increased obviously when the line passes through the precipitate (Fig. 13b), indicating that the precipitates exhibit a delayed oxidation.

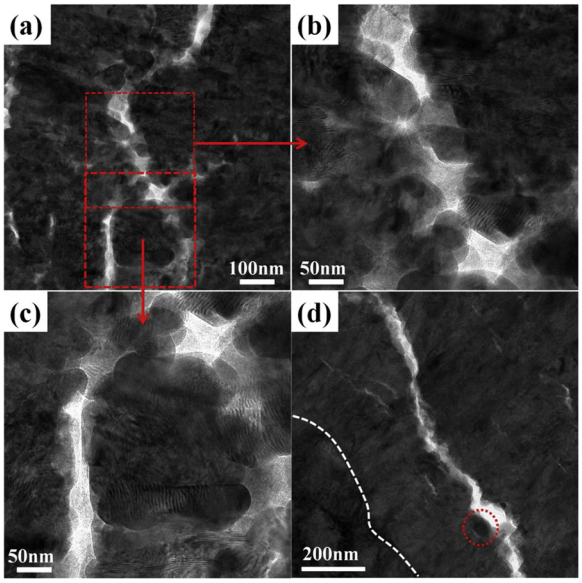

Fig. 14. Representative TEM images of the cross-sectional morphology of oxide films in sample 2 after 200 days' exposure time: (a) a long crack passes through the oxide films; (b)–(c) high magnification TEM images for the square region marked in (a); (d) a precipitate is exactly located along the crack path. (For interpretation of the references to colour in the text, the reader is referred to the web version of this article.)

The volume of precipitates will not change, while the oxide scales around it will dilate because of the high BP ratio (1.56 for Zr/ZrO_2). The oxide will expand outward because the compressive stress decreases towards the outer surface in the oxide, so the micro-cracks will form above the precipitates.

Finally, the two mechanisms for crack formation occur simultaneously and play crucial roles together during the oxidation process for zirconium alloys. Fig. 14 shows the typical TEM morphology of the oxide grains near a long crack. It is clear that along the undulated crack, some equiaxed grains are observed with size of 30–50 nm (Fig. 14b and c). The long cracks destroy the integrity of the columnar grain and allows for the transition from columnar to equiaxed grains. Meanwhile, it is noting that some precipitates are exactly situated along the crack path, as marked by red circles (Fig. 14d). It is therefore concluded that the long cracks are formed by the inter-connection of short cracks, which are caused by the phase transformation from tetragonal to monoclinic and the delayed oxidation of precipitates. The long cracks allow for the ingression of pure water through the oxide and finally result in the occurrence of transition.

4.2. Effect of annealing temperature on the anti-corrosion properties

It is commonly accepted that the oxidation process of zirconium alloys is mainly controlled by the rate of diffusing species through the oxide layer to the O/M interface [14,58]. The effective diffusion coefficient of oxygen in the zirconium alloys can be expressed by Hart's law [67]:

$$D_{eff} = (1 - f)D_L + f \cdot D_{gb} \quad (1)$$

where D_L and D_{gb} respectively represent the diffusion coefficient for lattice and grain boundary and f is the density of grain boundaries per unit area, which can be formulated by the equation:

$$f = \frac{2\delta}{d} \quad (2)$$

where δ corresponds to the grain boundary thickness and is typically ~0.5 nm [68], and d corresponds to the alloy grain size. According to the classical work of Richie [69], the numerical values of the diffusion parameters D_L and D_{gb} can be identified by the relations:

$$D_L = 2.747 \times 10^{-6} \exp(-\frac{180835}{RT}) \quad (3)$$

$$D_{gb} = 6.998 \times 10^{-11} \exp(-\frac{91896}{RT}) \quad (4)$$

where R is the ideal gas constant and T is the diffusion temperature ranges from 290 to 650 °C. Thus, the diffusion rate of oxygen in zirconium can be calculated using Eq. (3) with the consideration temperature of 360 °C ($D_L = 3.28 \times 10^{-21}$; $D_{gb} = 1.82 \times 10^{-18}$). It can be seen that grain boundary diffusion for oxygen is approximately 500 times faster than lattice diffusion.

At the initial stage of corrosion, the oxidation rate in both groups is very high due to the direct contact of metal with water at high temperature and high pressure. The oxidation rate at this stage is determined by the effective diffusion coefficient of oxygen in the alloys, which can also be estimated by Eqs. (1)–(4). Here, the parameter d used in the calculation is derived from the EBSD data for both groups. The average grain size of alloy is used in both samples for approximate calculation (2.8 μm and 1.5 μm for sample 1 and 2, respectively). Consequently, the effective diffusion coefficient of oxygen in sample 1 is 3.928×10^{-21} at the initial stage of oxidation, while this value is 4.491×10^{-21} in sample 2. From a theoretical point of view, it means that diffusion of oxygen within the metallic substrate is then quicker for sample 2, with a much higher fraction of grain boundary in the metal (Fig. 2b). Although the weight gains of samples at the very beginning of oxidation are not clear, it still can be estimated by the first measure point of corrosion test. The oxidation rates (defined as the slope of the weight gain curve in Fig. 3) are respectively 3.19 $mg \cdot dm^{-2} day^{-1}$ and 4.28 $mg \cdot dm^{-2} day^{-1}$ for sample 1 and 2 after 3 days' exposure. This results show that the oxidation rate in sample 2 is much higher than that in sample 1 at the early stage of oxidation, which agrees qualitatively well with theoretical approach previously shown.

As the oxidation progresses, a dense and well-oriented columnar grains begin to form, and the grain boundary area and the mis-orientation between grains are reduced. The oxidation rate at this time is determined by the microstructure of oxide, especially by the grain boundary area of oxide. Fig. 15 shows the typical oxide microstructure at the O/M interface region of Zr-Sn-Nb-Fe-Mo alloy annealed at 480 and 550 °C after 200 days' exposure. The size of the columnar grains in both groups was counted from the TEM images. To ensure the reliability of the statistical results, at least 20 images from each sample were counted. The detail information is listed in Table 2. A columnar grain average width/length of 38/170 nm in oxide is obtained in sample 2, and 79/210 nm in sample 1. The larger columnar oxide grain in sample 1 will result in the reduction of grain boundary area, thus the effective diffusion coefficient of oxygen will decrease in the oxide, finally leading to a lower oxidation kinetics. Previous work [70] suggested that the termination of columnar grain growth is attributed to the small mismatches in the orientation of adjacent grains, leading to the stress accumulation. Sample 1 is annealed by a higher annealing temperature, so a relatively higher recrystallization degree of alloy is obtained. EBSD

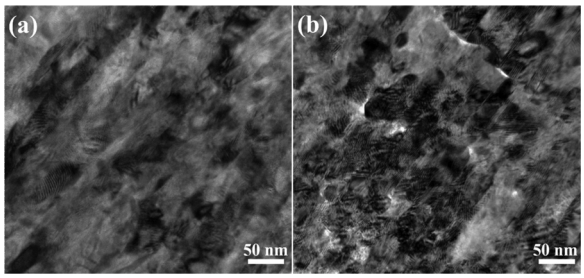

Fig. 15. Microstructure of the oxide/metal interface region in the oxide at 360 °C/18.6 MPa after 200 days' exposure time: (a) sample 1 and (b) sample 2.

Table 2
Statistical data about oxide columnar grain size at O/M interface from TEM images after 200 days' exposure in both samples.

Alloy	Average width/Range (nm)	Average length/Range (nm)
Sample 1	79/(37–144)	210/(88–515)
Sample 2	38/(16–70)	170/(73–358)

data shows that the fraction of LAGBs in sample 1 (50.7%) is much lower than that in sample 2 (81.3%), thus fewer defects such as dislocations are existed in sample 1. It is likely possible that a reduced degree of defects in metal will cause an improved degree of alignment in the growing grains, which will be able to grow further to larger grain size.

4.3. Possible mechanism relating to the oxidation process

The oxidation resistance of zirconium alloys is one of the main issues for their use as fuel cladding material in nuclear plants, which is mainly dependent on microstructure and composition. Based on the discussion above, the proceeding model for the oxidation process of zirconium alloys corroding in pure water at 360 °C is schematically shown in Fig. 16. For sample 1 with partial recrystallization degree (Fig. 16a), a thin layer (300–500 nm) is formed with small equiaxed grains on the matrix at the initial stage of oxidation. Harlow [63] studied the initial oxidation behavior by *in-situ* TEM techniques and suggested that the oxide formed as a mixture of monoclinic and tetragonal phase, and some HCP Zr remaining. Therefore, it can be concluded that both monoclinic and tetragonal grains will nucleate in this thin layer and a high volume fraction of tetragonal grains will be stabilized by the small grain size [51]. The compressive stress is not high as the oxide film at this time is thin (300–500 nm). The oxidation rate is high owing to the porous microstructure of these newly formed equiaxed grains and the moderate density of dislocations in the matrix. As the oxide grows inwards, the favorably oriented grains will grow into large columnar grains at the interface. The columnar structures are composed of tetragonal and monoclinic phases, and can grow to a certain length. The small favorably oriented tetragonal grains will be allowed to grow to the critical size, depending on the compressive stress distribution in the oxide. In this case, the oxidation rate is relatively low, owing to the protective nature of these well-oriented columnar structures. As is shown in Fig. 11a, the stress distribution in the oxide is not uniform, and a stress gradient is obtained from O/M interface to outer surface. The stress magnitude is maximum at the O/M interface, especially above the peak of undulating interface [71]. Thus, when the compressive stress in a particular region of zirconia decreases to a critical level away from the interface, the well-developed tetragonal grains in that region will transform to monoclinic grains. The volume expansion and shear strain associated with the tetragonal-monoclinic transformation causes the formation of cracking and porosity, which would provide a fast track for diffusing species [64]. Meanwhile, the delayed oxidation of the precipitate allows for the formation of crescent shaped micro-cracks on the top of itself. Idarraga's work [43] found local stress relaxation close to cracks by Raman spectroscopy, so it is likely possible that the local stress relaxation caused by these micro-cracks will result in the tetragonal-monoclinic transformation, further leading to cracks and porosity.

As the oxidation continues, more cracks will generate and link up with pre-existing porosity and cracking in the oxide scales, providing interconnected paths for oxygen or hydrogen to penetrate near the O/M

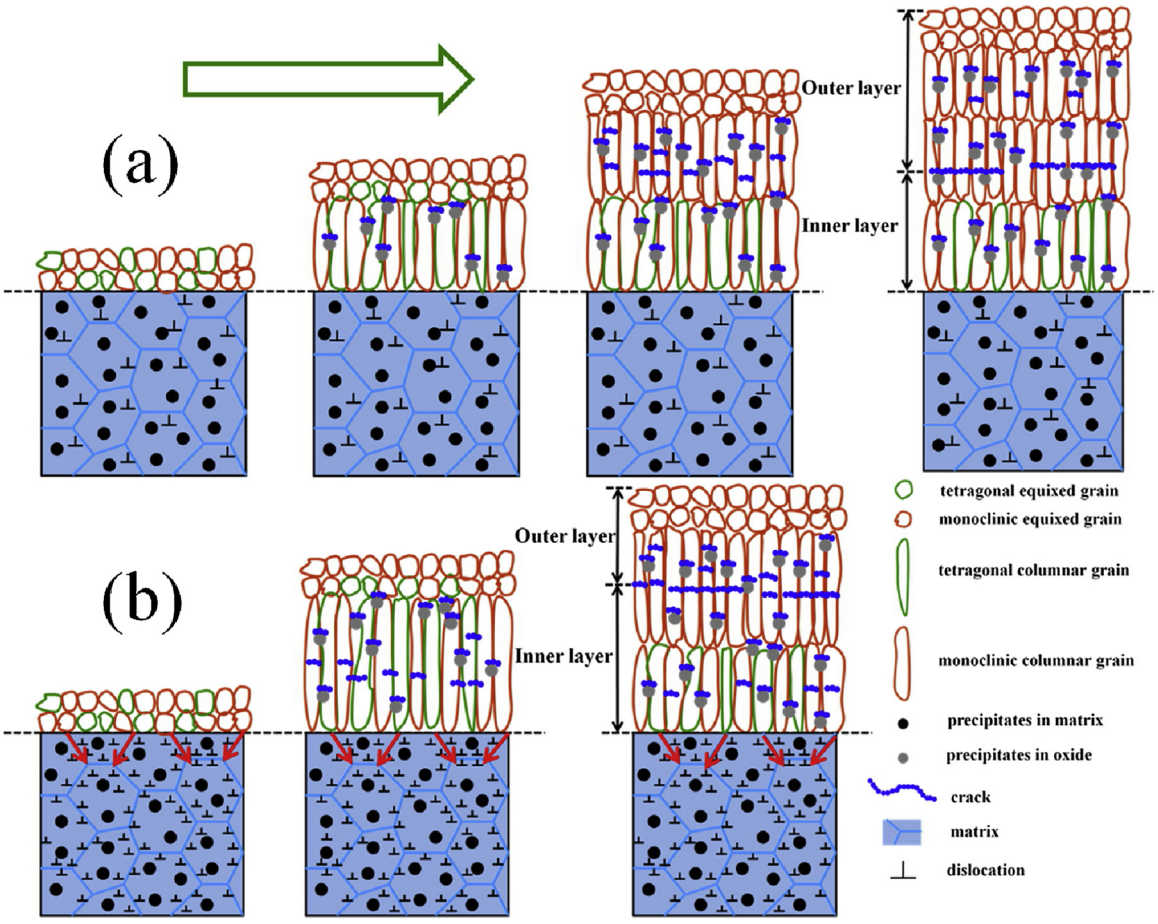

Fig. 16. Schematic drawings for the oxide grain growth process on both groups in pure water at 360 °C/18.6 MPa: (a) sample 1 and (b) sample 2.

interface. The inter-connected long cracks will finally lead to the layering of oxides. Therefore, the transition occurs in oxidation kinetics, corresponding to a relatively abrupt increase in weight gain. The long cracks also promote the stress relaxation and could destroy the integrity of oxide, resulting in transition from columnar to equiaxed grains. After the transition, the entire oxidation process restarts and the periodic oxidation kinetics occur. As for sample 2, a lower degree of re-crystallization is obtained owing to the relatively lower annealing temperature. Thus, more defects are existed in the metal, such as dislocations and sub-grains. The oxidation rate is relatively higher due to an improved fraction of grain boundary area, as the grain boundaries are the most common short-circuiting paths for diffusion. Therefore, as shown in Fig. 16b, more cracks will be generated in the oxide films, leading to the earlier delamination of oxides.

5. Conclusion

A detailed investigation on the microstructure and stress distribution of oxide scales formed on a Zr-Sn-Nb-Fe-Mo alloy at 360 °C/18.6 MPa for 300 days has been performed in order to establish some correlations between microstructure and anti-corrosion properties. The results presented in this work give an insight on the corrosion mechanism of zirconium alloys. The main conclusions are as follows:

(1) The alloy shows a much higher corrosion resistance when heat treated at 550 °C/5 h in pure water at 360 °C/18.6 MPa, compared with that heat treated at 480 °C/5 h. The improved degree of re-crystallization of alloy causes the reduction of grain boundary area, thereby reducing the oxidation rate.
(2) Two mechanisms are responsible for the formation of cracks in the oxide: one is the phase transformation from tetragonal to monoclinic; the other is the delayed oxidation of precipitates.
(3) As the oxidation progresses, cracks increase and link together to form long cracks, leading to the layering of the oxide scales.

Data availability statement

The raw/processed data required to reproduce these findings cannot be shared at this time as the data also forms part of an ongoing study.

Acknowledgements

The authors are grateful to the financial support of the National Natural Science Foundation of China (Grant Nos: U1602274, 51741108, 51371114, 51875349, 51501112), the 111 Project (Grant No. B16032) and the Laboratory Innovative Research Program of Shanghai Jiao Tong University (Grant No. 17SJ-14).

References

[1] A.T. Motta, Waterside corrosion in zirconium alloys, JOM 63 (2011) 59–63.
[2] A.T. Motta, A. Couet, R.J. Comstock, Corrosion of zirconium alloys used for nuclear fuel cladding, Annu. Rev. Mater. Res. 45 (2015) 311–343.
[3] B. Cox, Some thoughts on the mechanisms of in-reactor corrosion of zirconium alloys, J. Nucl. Mater. 336 (2005) 331–368.
[4] D. Charquet, Improvement of the uniform corrosion resistance of Zircaloy-4 in the absence of irradiation, J. Nucl. Mater. 160 (1988) 186–195.
[5] N. Ni, S. Lozano-Perez, J. Sykes, C. Grovenor, Quantitative EELS analysis of zirconium alloy metal/oxide interface, Ultramicroscopy 111 (2011) 123–130.
[6] D. Hudson, A. Cerezo, G.D.W. Smith, Zirconium oxidation on the atomic scale, Ultramicroscopy 109 (2009) 667–671.
[7] K.J. Annand, I. MacLaren, M. Gass, Utilising dual EELS to probe the nanoscale mechanisms of the corrosion of Zircaloy-4 in 350 °C pressurized water, J. Nucl. Mater. 465 (2015) 390–399.
[8] Z. Wang, B.X. Zhou, B. Chen, W. Zhu, B. Wen, L. Wu, H.K. Tang, Z.Q. Fang, Q. Li, M.Y. Yao, In-situ oxidation and short-time corrosion investigation on strain and dislocation during the generation and growth of ZrO_2, Corros. Sci. 122 (2017) 26–31.
[9] A. Couet, A.T. Motta, A. Ambard, D. Livigni, In-situ electrochemical impedance spectroscopy measurements of zirconium alloy oxide conductivity: relationship to hydrogen pickup, Corros. Sci. 119 (2017) 1–13.
[10] N. Pétigny, P. Barberis, C. Lemaignan, Ch. Valot, M. Lallemant, In situ XRD analysis of the oxide layers formed by oxidation at 743 K on Zircaloy 4 and Zr-1NbO, J. Nucl. Mater. 280 (2000) 318–330.
[11] G. Zumpicchiat, S. Pascal, M. Tupin, C. Berdin-Méric, Finite element modelling of the oxidation kinetics of Zircaloy-4 with a controlled metal-oxide interface and the influence of growth stress, Corros. Sci. 100 (2015) 209–221.
[12] A. Couet, A.T. Motta, A. Ambard, The coupled current charge compensation model for zirconium alloy fuel cladding oxidation: I. Parabolic oxidation of zirconium alloys, Corros. Sci. 100 (2015) 73–84.
[13] B.D.C. Bell, S.T. Murphy, P.A. Burr, R.J. Comstock, J.M. Partezana, R.W. Grimes, M.R. Wenman, The influence of alloying elements on the corrosion of Zr alloys, Corros. Sci. 105 (2016) 36–43.
[14] S.S. Yardley, K.L. Moore, N. Ni, J.F. Wei, S. Lyon, M. Preuss, S. Lozano-Perez, C.R.M. Grovenor, An investigation of the oxidation behaviour of zirconium alloys using isotopic tracers and high resolution SIMS, J. Nucl. Mater. 443 (2013) 436–443.
[15] M. Preuss, P. Frankel, S. Lozano-Perez, D. Hudson, E. Polatidis, N. Ni, J. Wei, Studies regarding corrosion mechanisms in zirconium alloys, J. ASTM Int. 8 (2011) 649–681.
[16] P. Bossis, G. Lelikvre, P. Barberis, X. Iltis, F. Lefebvre, Multi-scale characterization of the metal-oxide interface of zirconium alloys, J. ASTM Int. (2000) 918–942.
[17] A. Garner, J. Hu, A. Harte, P. Frankel, C. Grovenor, S.L. Perez, M. Preuss, The effect of Sn concentration on oxide texture and microstructure formation in zirconium alloys, Acta Mater. 99 (2015) 259–272.
[18] J. Wei, P. Frankel, E. Polatidis, M. Blat, A. Ambard, R.J. Comstock, L. Hallstadius, D. Hudson, G.D.W. Smith, C.R.M. Grovenor, M. Klaus, R.A. Cottis, S. Lyon, M. Preuss, The effect of Sn on autoclave corrosion performance and corrosion mechanisms in Zr-Sn-Nb alloys, Acta Mater. 61 (2013) 4200–4214.
[19] B.D.C. Bell, S.T. Murphy, P.A. Burr, R.W. Grimes, M.R. Wenman, The effect of Nb on the corrosion and hydrogen pick-up of Zr alloys, Acta Mater. 132 (2017) 425–431.
[20] S. Müller, L. Lanzani, Corrosion of Zr-1Nb and Zr-2.5Nb in 0.1 M LiOH at 343 °C, Procedia Mater. Sci. 8 (2015) 46–55.
[21] L.Y. Chen, P. Shen, L. Zhang, S. Lu, L.J. Chai, Z. Yang, L.C. Zhang, Corrosion behavior of non-equilibrium Zr-Sn-Nb-Fe-Cu-O alloys in high temperature 0.01 M LiOH aqueous solution and degradation of the surface oxide films, Corros. Sci. 136 (2018) 221–230.
[22] W.J. Gong, H.L. Zhang, C.F. Wu, H. Tian, X.T. Wang, The role of alloying elements in the initiation of nanoscale porosity in oxide films formed on zirconium alloys, Corros. Sci. 77 (2013) 391–396.
[23] J. Huang, M.Y. Yao, B. Chen, Y. Mao, X. Liang, J.L. Zhang, B.X. Zhou, Q. Li, Oxidation behavior of Zr_9S_2 precipitates in Zr-0.8Sn-1.0Nb-0.3Fe-0.1Cr-xS alloys, Corros. Sci. 120 (2017) 82–89.
[24] H.G. Shi, X.L. Guo, J.X. Li, J.W. Mao, W.J. Lu, Effects of Mn addition on the corrosion behaviors of Zr-Sn-Nb-Fe-Mo alloys, Corros. Sci. 157 (2019) 167–179.
[25] L.Y. Chen, J.X. Li, Y. Zhang, L.C. Zhang, W.J. Lu, L.F. Zhang, L.Q. Wang, D. Zhang, Effects of alloyed Si on the autoclave corrosion performance and periodic corrosion kinetics in Zr-Sn-Nb-Fe-O alloys, Corros. Sci. 100 (2015) 651–662.
[26] G.P. Sabol, ZIRLO™—an alloy development success, J. ASTM Int. 2 (2005) 3–24.
[27] A. Couet, A.T. Motta, R.J. Comstock, Effect of alloying elements on hydrogen pickup in zirconium alloys, J. ASTM Int. (2005) 479–514.
[28] D.F. Taylor, Microstructural aspects of Zircaloy nodular corrosion in steam, J. Nucl. Mater. 277 (2000) 295–314.
[29] N.V. Bangaru, An investigation of the microstructures of heat-treated Zircaloy-4, J. Nucl. Mater. 131 (1985) 280–290.
[30] B. Cox, H.I. Sheikh, Redistribution of the alloying elements during Zircaloy-2 oxidation, J. Nucl. Mater. 249 (1997) 17–32.
[31] D. Charquet, Influence of precipitate density on the nodular corrosion resistance of Zr-Sn-Fe-Cr alloys at 500 °C, J. Nucl. Mater. 288 (2001) 237–240.
[32] M. Pahutová, K. Kuchařová, J. Čadek, Martensitic zirconium alloys: influence of chemical composition on creep characteristics, J. Nucl. Mater. 131 (1985) 20–31.
[33] H.L. Yang, S. Kano, Y. Matsukawa, Y.F. Li, J.J. Shen, Z.S. Zhao, F. Li, Y. Satoh, H. Abe, Study on recrystallization and correlated mechanical properties in Mo-modified Zr-Nb alloys, Mater. Sci. Eng. A 661 (2016) 9–18.
[34] J.H. Lee, S.K. Hwang, Effect of Mo addition on the corrosion resistance of Zr-based alloy in water containing LiOH, J. Nucl. Mater. 321 (2003) 238–248.
[35] M.Y. Yao, Y.F. Shen, Q. Li, J.C. Peng, B.X. Zhou, J.L. Zhang, The effect of final annealing after β-quenching on the corrosion resistance of Zircaloy-4 in lithiated water with 0.04 M LiOH, J. Nucl. Mater. 435 (2013) 63–70.
[36] N. Ni, S. Lozano-Perez, J.M. Sykes, G.D.W. Smith, C.R.M. Grovenor, Focussed ion beam sectioning for the 3D characterization of cracking in oxide scales formed on commercial ZIRLO™ alloys during corrosion in high temperature pressurized water, Corros. Sci. 53 (2011) 4073–4083.
[37] H.G. Kim, I.H. Kim, B.K. Choi, J.K. Park, Y.H. Jeong, K.T. Kim, Study of the corrosion and microstructure with annealing conditions of a β-quenched HANA-4 alloy, Corros. Sci. 52 (2010) 3162–3167.
[38] J.Y. Park, B.K. Choi, S.J. Yoo, Y.H. Jeong, Corrosion and oxide properties of HANA alloys, J. ASTM Int. 5 (2008) 471–485.
[39] R.M. Langford, C. Clinton, In situ lift-out using a FIB-SEM system, Micron 35 (2004) 607–611.
[40] L.A. Giannuzzi, F.A. Stevie, A review of focused ion beam milling techniques for TEM specimen preparation, Micron 30 (1999) 197–204.
[41] N. Ni, D. Huson, J. Wei, P. Wang, S. Lozano-Perez, G.D.W. Smith, J.M. Sykes, S.S. Yardley, K.L. Moore, S. Lyon, R. Cottis, M. Preuss, C.R.M. Grovenor, How the crystallography and nanoscale chemistry of the metal/oxide interface develops during the aqueous oxidation of zirconium cladding alloys, Acta Mater. 60 (2012)

7132–7149.
[42] I. Idarraga, M. Mermoux, C. Duriez, A. Crisci, J.P. Mardon, Raman investigation of pre- and post-breakaway oxide scales formed on Zircaloy-4 and M5® in air at high temperature, J. Nucl. Mater. 421 (2012) 160–171.
[43] I. Idarraga, M. Mermoux, C. Duriez, A. Crisci, J.P. Mardon, Potentialities of Raman imaging for the analysis of oxide scales formed on Zircaloy-4 and M5 in air at high temperature, Oxid. Met. 79 (2013) 289–302.
[44] P. Barberis, T. Merle-Méjean, P. Quintard, On Raman spectroscopy of zirconium oxide films, J. Nucl. Mater. 246 (1997) 232–243.
[45] M. Mamivand, M.A. Zaeem, H.E. Kadiri, L.Q. Chen, Phase field modeling of the tetragonal-to-monoclinic phase transformation in zirconia, Acta Mater. 61 (2013) 5223–5235.
[46] H.E. Kadiri, Z.N. Utegulov, M. Khafizov, M.A. Zaeem, M. Mamivand, A.L. Oppedal, K. Enakoutsa, M. Cherkaoui, R.H. Graham, A. Arockiasamy, Transformation and cracks in zirconia films leading to breakaway oxidation of Zircaloy, Acta Mater. 61 (2013) 3923–3935.
[47] B. Panicaud, J.L. Grosseau-Poussard, D. Retraint, M. Guérain, L. Li, On the mechanical effects of a nanocrystallisation treatment for ZrO_2 oxide films growing on a zirconium alloy, Corros. Sci. 68 (2013) 263–274.
[48] M. Blat-Yrieix, A. Ambard, F. Foct, A. Miquet, S. Beguin, N. Cayet, Toward a better understanding of dimensional changes in zircaloy-4: what is the impact induced by hydrides and oxide layer? J. ASTM Int. 5 (2008) 101321.
[49] J. Chevalier, L. Gremillard, A.V. Virkar, D.R. Clarke, The tetragonal-monoclinic transformation in zirconia: lessons learned and future trends, J. Am. Ceram. Soc. 92 (2009) 1901.
[50] W. Qin, C. Nam, H.L. Li, J.A. Szpunar, Effects of local stress on the stability of tetragonal phase in ZrO_2 film, J. Alloys Compd. 437 (2007) 280–284.
[51] W. Qin, C. Nam, H.L. Li, J.A. Szpunar, Tetragonal phase stability in ZrO_2 film formed on zirconium alloys and its effects on corrosion resistance, Acta Mater. 55 (2007) 1695–1701.
[52] P. Bouvier, Etude Raman des distributions de phase et de contrainte dans des couches d'oxydation d'alliages de Zirconium, Ph.D. Thesis, Institut National Polytechnique de Grenoble, France, 2000.
[53] J. Godlewski, P. Bouvier, G. Lucazeau, L. Fayette, Stress distribution measured by Raman spectroscopy in zirconia films formed by oxidation of Zr-based alloys, ASTM STP 1354 (2000) 877–900.
[54] E. Polatidis, P. Frankel, J. Wei, M. Klaus, R.J. Comstock, A. Ambard, S. Lyon, R.A. Cottis, M. Preuss, Residual stresses and tetragonal phase fraction characterization of corrosion tested Zircaloy-4 using energy dispersive synchrotron X-ray diffraction, J. Nucl. Mater. 432 (2013) 102–112.
[55] P. Barberis, V. Rebeyrolle, J.J. Vermoyal, V. Chabretou, J.P. Vassault, CASTA DIVA: experiments and modeling of oxide-induced deformation in nuclear components, ASTM STP 1505 (2007) 612–631.
[56] H. Buscail, R. Rolland, C. Issartel, S. Perrier, L. Latu-Romain, Stress determination by in-situ X-ray diffraction—influence of water vapour on the Zircaloy-4 oxidation at high temperature, Corros. Sci. 134 (2018) 38–48.
[57] P. Platt, E. Polatidis, P. Frankel, M. Klaus, M. Gass, R. Howells, M. Preuss, A study into stress relaxation in oxides formed on zirconium alloys, J. Nucl. Mater. 456 (2015) 415–425.
[58] N. Ni, S. Lozano-Perez, M.L. Jenkins, C. English, G.D.W. Smith, J.M. Sykes, C.R.M. Grovenor, Porosity in oxides on zirconium fuel cladding alloys, and its importance in controlling oxidation rates, Scr. Mater. 62 (2010) 564–567.
[59] N. Ni, S. Lozanoperez, J.M. Sykes, G.D. Smith, C.R.M. Grovenor, Focussed ion beam sectioning for the 3D characterisation of cracking in oxide scales formed on commercial ZIRLO™ alloys during corrosion in high temperature pressurised water, Corros. Sci. 53 (2011) 4073–4083.
[60] P. Platt, S. Wedge, P. Frankel, M. Gass, R. Howells, M. Preuss, A study into the impact of interface roughness development on mechanical degradation of oxides formed on zirconium alloys, J. Nucl. Mater. 459 (2015) 166–174.
[61] P. Kofstad, On the formation of porosity and microchannels in growing scales, Oxid. Met. 24 (1985) 265–276.
[62] A. Garner, A. Gholinia, P. Frankel, M. Gass, I. MacLacren, M. Preuss, The microstructure and microtexture of zirconium oxide films studied by transmission electron backscatter diffraction and automated crystal orientation mapping with transmission electron microscopy, Acta Mater. 80 (2014) 159–171.
[63] W. Harlow, H. Ghassemi, M.L. Taheri, Determination of the initial oxidation behavior of Zircaloy-4 by in-situ TEM, J. Nucl. Mater. 474 (2016) 126–133.
[64] P. Platt, P. Frankel, M. Gass, R. Howells, M. Preuss, Finite element analysis of the tetragonal to monoclinic phase transformation during oxidation of zirconium alloys, J. Nucl. Mater. 454 (2014) 290–297.
[65] P. Bossis, J. Thomazet, F. Lefebvre, Study of the mechanisms controlling the oxide growth under irradiation: characterization of irradiated Zircaloy-4 and Zr-1Nb-O oxide scales, ASTM STP 1423 (2002) 190–221.
[66] C. Proff, S. Abolhassani, C. Lemaignan, Oxidation behaviour of binary zirconium alloys containing intermetallic precipitates, J. Nucl. Mater. 416 (2011) 125–134.
[67] E.W. Hart, On the role of dislocations in bulk diffusion, Acta Metall. 5 (1957) 595.
[68] X. Peng, J. Yan, Y. Zhou, F. Wang, Effect of grain refinement on the resistance of 304 stainless steel to breakaway oxidation in wet air, Acta Mater. 53 (2005) 5079–5088.
[69] I.G. Ritchie, A. Atrens, The diffusion of oxygen in alpha-zirconium, J. Nucl. Mater. 67 (1977) 254–264.
[70] A.T. Motta, A. Yilmazbayhan, R.J. Comstock, J. Partezana, G.P. Sabol, B. Lai, Z.H. Cai, Microstructure and growth mechanism of oxide layers formed on Zr alloys studied with micro-beam synchroton radiation, J. ASTM Int. 2 (2005) 205–232.
[71] P. Platt, P. Frankel, M. Gass, M. Preuss, Critical assessment of finite element analysis applied to metal-oxide interface roughness in oxidizing zirconium alloys, J. Nucl. Mater. 464 (2015) 313–319.